Flow and heat transfer measurements in natural convection in coarse-grained porous media

Ataei-Dadavi, Iman; Chakkingal, Manu; Kenjeres, Sasa; Kleijn, Chris R.; Tummers, Mark J.

DOI
10.1016/j.ijheatmasstransfer.2018.10.118

Publication date
2019

Document Version
Accepted author manuscript

Published in
International Journal of Heat and Mass Transfer

Flow and Heat Transfer Measurements in Natural Convection in Coarse-grained Porous Media

I. Ataei-Dadavi[a,*], M. Chakkingal[a], S. Kenjeres[a], C.R. Kleijn[a], M.J. Tummers[b]

[a] *Transport Phenomena Section, Department of Chemical Engineering, Delft University of Technology, Van der Maasweg 9, 2629HZ Delft, The Netherlands*
[b] *Fluid Mechanics Section, Department of Process and Energy, Delft University of Technology, Leeghwaterstraat 39, 2628CB Delft, The Netherlands*

Abstract

This paper reports on an experimental study of natural convection in an enclosure that is heated at the bottom and cooled at the top, filled with a packed bed of relatively large solid spheres. Nusselt numbers were measured for various sphere conductivities, spheres sizes and sphere packings for Rayleigh numbers varying between 10^7 and 10^9. The Nusselt number measurements showed that at lower Rayleigh numbers, the heat transfer is lower than that for pure Rayleigh-Bénard convection, with the difference depending on packing type, size, and conductivity of the spheres. However, at high Rayleigh numbers, there exists an asymptotic regime where the convective contribution of the total heat transfer for all sphere conductivities, sizes, and packing types collapse on a single curve which is very close to the curve for pure Rayleigh-Bénard convection. Refractive index-matching of the fluid and the solid spheres enabled the use of particle image velocimetry and liquid crystal thermography to obtain highly resolved velocity and temperature fields. The comparison of the velocity and temperature fields for the two heat transfer regimes showed that the velocity magnitudes inside the pores in the core region are much higher in the asymptotic regime than those in the low Rayleigh number regime, which lead to a deeper penetration of cold and hot fluid elements and higher heat transfer.

Keywords: Natural Convection; Porous media; Heat transfer; Particle Image Velocimetry; Liquid Crystal Thermography.

1. Introduction

Natural convection in porous media plays an important role in a range of physical and industrial applications such as steel and iron production, geothermal energy, chemical industries, oil production, and hydrogeology and therefore has attracted a great deal of attention. The most widely studied configuration in this field is that of a fluid-saturated porous medium bounded between two horizontal impermeable walls with the lower wall hotter than the upper one. A large number of numerical and theoretical studies have focused on modeling flow and heat transfer in this configuration. The frequently used Darcy model [1–3] assumes that inertia is negligible compared to viscous effects, and that the flow and thermal length scales are much larger than porous length scales. Other studies added inertia terms [4] or a quadratic drag term (Forchheimer equation) [5] to the Darcy model. Relatively few experimental studies have been performed to verify these models and most of them were only dedicated to heat transfer measurements at low Rayleigh numbers using fine grains where the Darcy assumptions hold [4,6,7].

In coarse-grained porous media, the length scales of the solid porous material are not small compared to the flow and thermal length scales in the fluid. This results in complex interactions between the flow and the solid, and the Darcy model is no longer valid. Very few experimental studies have been conducted using coarse-grained porous media. Kladias and Prasad [8] measured heat transfer in packed beds of spheres of varying bead diameters, solid materials, and fluids to validate the Darcy-Brinkman-Forchheimer (DBF) flow model. They observed that the DBF solutions are in agreement with the experimental results only at low Ra-numbers and for small spheres (low Darcy numbers). Keene and Goldstein [9] studied heat transfer across a 279×279×279 mm^3 cubical cell filled with 25.4 mm spherical polypropylene beads in simple cubic packing. They achieved high fluid Ra-numbers $1.68\times10^9 < Ra < 3.86\times10^{11}$ by using compressed argon as the saturating fluid with pressure varying from 5.6 to 77 bar. They also employed the data sets from [8] and reported that at high Ra-numbers the heat transfer in porous media asymptotes to the behavior of a homogeneous fluid layer, unless the solid phase is highly conductive. Despite these studies, the heat transfer characteristics of natural convection in coarse-grained porous media still leave many open questions. In particular, the effect of the conductivity of spheres, packing structure of the porous matrix, and size of the spheres have not been systematically characterized and understood in terms of Nusselt vs. Rayleigh (Nu-Ra) relations for different flow regimes.

To explain the behavior of Nu-Ra data of natural convection in porous media, and to obtain a deeper understanding of the underlying physics, it is important to study the fluid flow at the pore scale. Previous experimental studies on natural convection in porous media mainly focused on the overall heat transfer, and data on the structure and dynamics of the flow and temperature fields are still lacking. Over the past decades, several researchers have attempted to visualize convection in porous media. The earliest studies were either qualitative flow visualizations [7,10,11] or single-point intrusive temperature measurements [12]. Shattuck et al. [13] were the first to measure velocity profiles of natural convection in a packed bed of 3.2 mm plastic beads heated from below. They were able to measure the vertically-averaged vertical velocity by using Magnetic Resonance Imaging (MRI). The most important drawback of their measurements was the limited spatial and temporal resolution.

* Corresponding author. *E-mail address:* i.ataeidadavi@tudelft.nl (I. Ataei-Dadavi)

Since Shattuck et al. velocity measurements of thermal convective flows inside porous media have not improved significantly, and highly resolved velocity fields have not been measured yet.

Optical flow measurement techniques such as Particle Image Velocimetry (PIV) for velocity measurements and Liquid Crystal Thermography (LCT) for temperature measurements cannot be used easily in porous media, because these methods obviously require optical access both for illumination and imaging of tracer particles. A possible approach to overcome this challenge is to match the refractive index of a (transparent) porous medium to that of the liquid. Refractive index matching has been applied in several studies to visualize fluid flow in porous media by minimizing image distortion and providing optical access. Two categories of liquids were considered to match the refractive index of transparent solid materials: (i) aqueous salt solutions [14,15], and (ii) organic fluids [16,17]. Unfortunately, the refractive indices of all frequently-used refractive index matched liquids are strongly temperature dependent. This adversely affects the refractive index matching and causes optical distortions in non-isothermal flows. As a consequence, all the refractive index matching works so far have been done only in isothermal flows and, to the knowledge of the authors, refractive index matched liquids have never been used to visualize thermal convection in porous media.

In this study, water was chosen as the liquid since its refractive index has the lowest sensitivity to temperature variations among all other refractive index matched liquids. Polyacrylamide hydrogel spheres were used to match the refractive index of water. A few recent studies have reported on the use of hydrogel and water for refractive index matching. Byron and Variano [18] and Weitzman et al. [19] fabricated solid objects from hydrogel material and explored the use of hydrogel for refractive index matching to study flow-solid interaction. Klein et al. [20] used hydrogel spherical particles in water to study the dynamics of inertial particles in a turbulent flow.

The main objective of the present study is to provide a better understanding of natural convection flow and heat transfer in wall-bounded coarse-grained porous media heated from below. To achieve this objective we carried out detailed heat transfer experiments for different sphere diameters, sphere thermal properties, and packing types. By matching the refractive index of the fluid and the spheres, optical measurement techniques like PIV and LCT could be applied to determine spatially and temporally resolved velocity and temperature fields in the cell.

2. Experimental Setup

2.1. Test Cell

The experiments were performed in two cubical convection cells with internal dimensions 77×77×77 mm^3 and 155×155×155 mm^3, see Fig. 1a. Each cell has copper top and bottom plates that serve as isothermal cold and hot walls, respectively. The four side walls are made of glass. The bottom plate is heated with electrical heating foils (Minco HK5955). The top plate is kept at a (relatively) low temperature by water from a thermostatic bath (Julabo FP51) that flows through channels, see Fig. 1a. In the heat transfer measurements, the side walls and the bottom plate are covered with polystyrene insulation panels of 30 mm thickness to minimize the heat losses to the surroundings. Pt100 resistance thermometers (Omega Engineering RTD-3-1PT100K2528-1M-T-1/10) with an inaccuracy of ±0.03 °C are used to measure the temperatures of the top and bottom plates. The temperature readings are collected by a data acquisition module (Omega Engineering PT-104A) and displayed in the logging software. Copper plates with very high thermal conductivity were used as the bottom and top plates to enhance the temperature uniformity of the plates. This was examined by measuring the temperature at different parts of the hot and cold plates. The maximum temperature non-uniformity observed was ~ 0.04 °C for the hot plate and ~ 0.01 °C for the cold plate. The average of two temperature sensors in each plate was used as the plate temperature. The temperature non-uniformity was considered in the calculation of the uncertainty of the temperature measurements (see Appendix A.).

2.2. Heat Transfer measurements

In the heat transfer measurements, the temperature difference between the bottom and top plates, ΔT, was varied between 2 °C and 20 °C in a number of steps. In each step, the electrical power fed to the heating foils, P, and the thermostatic bath temperature were adjusted. The temperatures of the top and bottom plates were then monitored in time until a steady state was reached. The temperature difference between the plates, ΔT, and the electrical power, P, were then measured. The temperatures of the hot and cold plates were always kept symmetrically around the ambient temperature of 22 °C to guarantee that the average Prandtl number of the working fluid remained constant during the experiment. This procedure also minimizes temperature differences between the cell and the ambient, thus minimizing heat losses to the surroundings. Taking into account the estimated heat conduction from the hot to the cold wall through the side walls, and neglecting heat losses to the surroundings since the side walls were well insulated and the average temperature of the cell $(T_{hot}+T_{cold})/2$ was kept equal to the ambient temperature, the overall Nusselt number Nu was computed from

$$\begin{aligned} \mathrm{Nu} &= (P - A_w k_w \Delta T/H) / (A_f k_f \Delta T/H) \\ &= P H/(A_f k_f \Delta T) - A_w k_w/(A_f k_f), \end{aligned} \quad (1)$$

where H is the distance between the top and bottom plates, and k_f and k_w are the thermal conductivities of the fluid and the side-wall material, respectively. A_f is the inner cross-sectional area of the cell and is equal to $A_f = H^2$, and A_w is the side-wall cross-sectional area and is equal to $A_w = 4w(H+w)$, where w is the side-wall thickness. The temperature difference ΔT was used to compute the Rayleigh number as in

$$\mathrm{Ra} = \beta \Delta T g H^3/(\alpha \nu), \quad (2)$$

where g is the gravitational acceleration, β is the thermal expansion coefficient, α is the thermal diffusion coefficient, and ν is the kinematic viscosity of the fluid. Note that the Nusselt number and the Rayleigh number defined in Eqs. (1) and (2) are based on fluid properties and not on properties of the porous medium. This is motivated by the observation that (for sufficiently high Ra-numbers) different heat transfer data sets group much better in Nu-number versus Ra-number

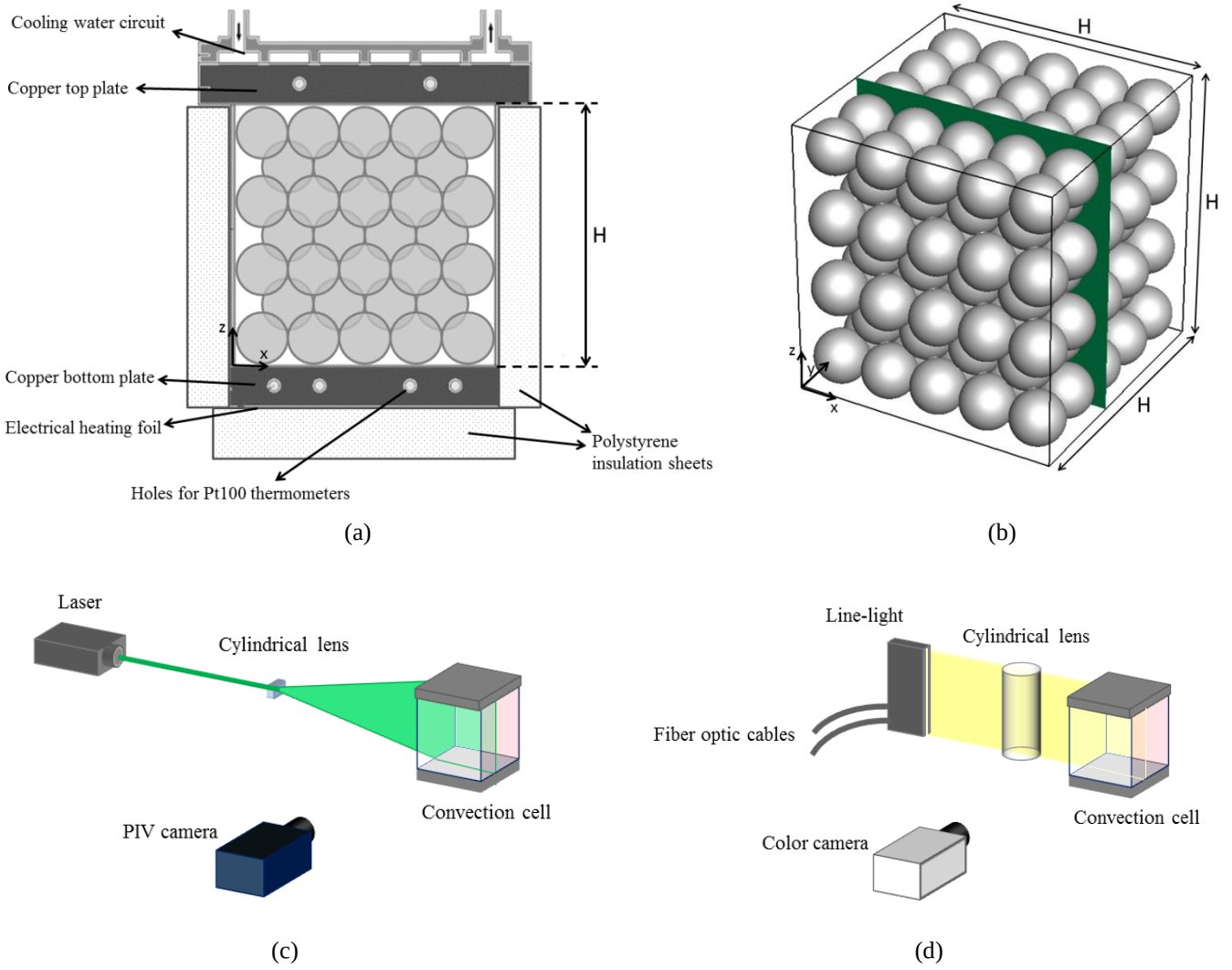

Fig. 1. (a) Schematic of the convection cell filled with spheres in BCT packing. (b) Schematic view of BCT packing and the PIV/LCT measurement plane. (c) Schematic of the PIV setup. (d) Schematic of the LCT setup.

graphs when fluid properties are used instead of porous medium properties. This was also observed by Keene and Goldstein [9].

The Ra-number was varied over the range $1.5\times10^7 \leq Ra \leq 1.5\times10^9$. The high Ra-numbers were achieved by either using methanol as a working fluid in the small cell (in heat transfer measurements), or by using water in the large cell (in PIV and LCT measurements). Water and methanol have similar Prandtl numbers; i.e. Pr = 6.75 for water and Pr = 7.63 for methanol (both at 22 °C). The maximum uncertainty in the heat transfer experiments occurs at the lowest temperature difference and is 2.8% for the Ra-number and 2.9% for the Nu-number (see Appendix A. for details).

In the heat transfer measurements, two different sphere diameters (10.5 mm and 15.3 mm) and four different sphere materials (brass, steel, glass, and polypropylene) were used. The spheres were arranged in a body-centered tetragonal (BCT) packing (see Fig. 1b), but simple cubic packing (SCP) and "random packings" were also considered.

2.3. PIV and LCT measurements

As mentioned above, refractive index matching is required to perform optical measurements (PIV and LCT) in porous media. To achieve this, water and hydrogel spheres were chosen as the working fluid and solid material, respectively. Hydrogel spheres are made of superabsorbent polymers and absorb more than 200 times their initial volume in water, resulting in a refractive index very close to that of the surrounding water (~0.1% difference).

Hydrogel spheres were arranged in BCT packing for PIV and LCT measurements. The measurement plane was located at y/H = 0.4 where y is the distance from the front wall, see Fig. 1b.

Particle Image Velocimetry (PIV) measurements were performed to obtain highly resolved 2D velocity fields. Fig. 1c shows the main components of the PIV setup. A diode-pumped solid-state laser (Pegasus) with a power of 0.8 W and a wavelength of 532 nm was used to create a light sheet with a thickness of approximately 2 mm. The flow was seeded with Polyamide tracer particles (Dantec Dynamics) with a mean diameter of 5 µm. A PIV camera (LaVision Imager Intense) with a resolution of 1376×1040 pixels was used to record images. The camera is equipped with a 28 mm Nikon lens with an f-number of 2.8. The magnification factor of the recordings is M = 0.083 for the small cell and M = 0.042 for the large cell. The resulting spatial resolution of images is around 80 µm/pixel for the small cell and 160 µm/pixel for the large cell. Raw PIV images were processed by commercial LaVision software (Davis 7.2). Velocity vectors were calculated based on a multi-pass cross-correlation with final interrogation windows of 16×16 pixels and an overlap of 50%

which corresponds to a vector resolution of 0.64 mm in the small cell, and 1.28 mm in the large cell. The laser was triggered with a pulse separation time of 60 ms, which leads to particle image displacement of about 6 pixels in the regions with the highest velocity.

Liquid Crystal Thermography (LCT) was used to visualize and obtain highly resolved temperature fields. The main components of the LCT setup are shown in Fig. 1d. Micro-encapsulated liquid crystal tracers (Hallcrest R25C60W) with a mean diameter of 10-15 μm were added to the working fluid with a concentration of 0.01 vol.%. The light source consisted of a LED lamp (Waldmann MCXFLS3) and a halogen lamp (Schott-Fostec, LLC). Since LED light is stronger in the range of lower wavelengths of the visible light spectrum (blue and green), whereas halogen light mostly contains higher wavelengths (yellow and red), the combination of the two lighting types gave a more uniform distribution of all colors in the visible spectrum. The light from these sources was transferred through fiber optic cables to a line-light (Schott-Fostec A08912). A cylindrical lens was then used to convert the diverging sheet coming from the line-light into a light sheet with a thickness of 2 mm inside the convection cell. A PCO Sensicam color camera with a resolution of 1280×1024 was used to record images of the liquid crystal particles.

In the LCT experiments, the reflected light was recorded in a direction normal to the light sheet, i.e. the viewing angle is 90° (see Fig. 1d). For this viewing angle, both the red start temperature and the bandwidth were reduced to about ~ 18.4 °C and ~ 11 °C, respectively. Therefore, the effective temperature range of the liquid crystals in this lightsheet configuration (with 90° viewing angle) was found to be from 18.4 °C to 29.4 °C. This $\Delta T = 11$ °C temperature difference leads to $Ra = 8.5\times10^7$ in the small cell and $Ra = 7.3\times10^8$ in the large cell. To determine quantitative temperature distributions from the recorded color images, a temperature-hue calibration was performed. Each calibration run involves imposing a constant temperature to both top and bottom plates, using a stirrer in the cell to ensure a uniform temperature, and at the same time monitoring the temperature of a Pt100 thermometer inserted into the cell. After achieving the steady state, the temperature was acquired by the thermometer and color images were taken to obtain the hue value. This was achieved by converting the recorded RGB images to HSV color space using the algorithm proposed by Smith [21] and extracting the hue component to generate a temperature-hue calibration curve. A sixth-order polynomial was fitted to the resulting calibration curve which then was used to obtain quantitative temperature fields. The uncertainty of the temperatures measured by LCT method was calculated to be around ± 0.5 °C.

3. Results and Discussion

3.1. Results of the Heat Transfer Measurements

Fig. 2 shows the Nu-Ra data-points for the BCT packing of glass spheres with 15.3 mm diameter measured in the small cell. As discussed in the previous section, the Nu-number and Ra-number are determined using fluid properties. The Nu-Ra data-points for pure Rayleigh-Bénard (RB) convection as determined in the same experimental setup, but in absence of the porous medium, are also shown in Fig. 2. In this figure, the closed and open markers represent results for experiments with water and methanol, respectively. The power-law that

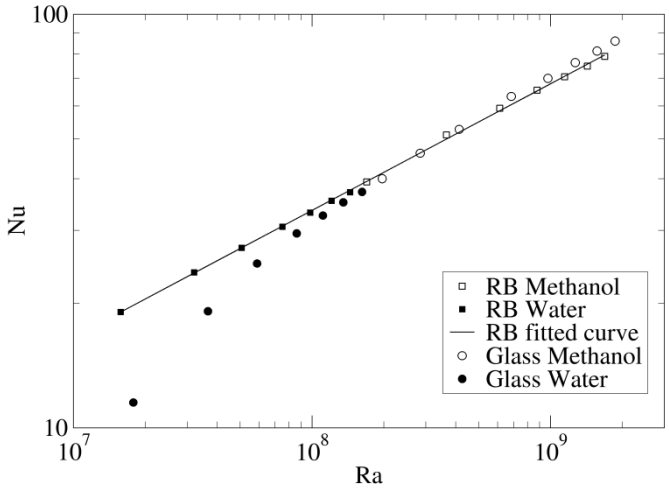

Fig. 2. Heat transfer data for BCT packing of $d = 15.3$ mm glass spheres, compared to that for pure Rayleigh-Bénard convection.

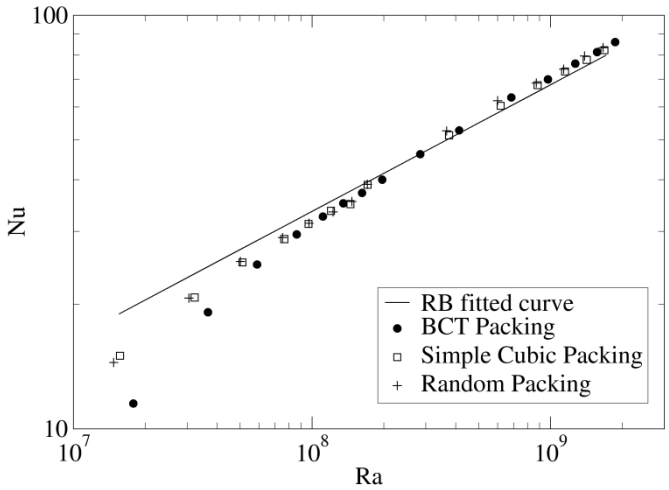

Fig. 3. Effect of packing type: heat transfer data for different packing structures of $d = 15.3$ mm glass spheres, compared to that for pure Rayleigh-Bénard convection.

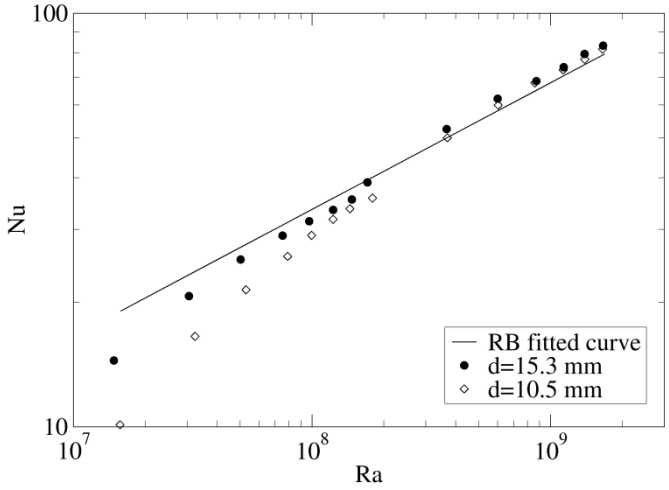

Fig. 4. Effect of size of spheres: heat transfer data for random packing of $d = 10.5$ mm and $d = 15.3$ mm glass spheres, compared to that for pure Rayleigh-Bénard convection.

best fits the RB data-points over the range of Ra-numbers between 1.5×10^7 and 1.5×10^9 was determined as $Nu = 0.119\ Ra^{0.306}$, which is in good agreement with the RB theoretical models and experimental data [22]. This relation is shown as a solid line in Fig. 2, and it serves as a reference in the remainder of the paper. Fig. 2 indicates that the presence of the glass spheres reduces the Nu-number (relative to the pure RB convection) at lower Ra-numbers. However, at high

Ra-numbers, the Nu-Ra data-points line up with and slightly exceed those for pure RB. This is in accordance with what Keene and Goldstein [9] observed in their experimental results.

3.1.1. Effect of Packing Type and Size of the Spheres

The effect of the packing type on the heat transfer was investigated by using three different packings of glass spheres with the same size in water and in methanol. The different packings have different porosities. For the studied small cubical cell, the BCT packing has a porosity ϕ = 0.420; the simple cubic packing has a porosity ϕ = 0.486; and the random packing has a porosity of ϕ = 0.454. The results shown in Fig. 3 demonstrate that at lower Ra-numbers, the heat transfer is the lowest for the BCT packing, which is less permeable to the fluid flow as compared to the other two packing types. However, at higher Ra-numbers, the Nu-Ra curves for all three packings converge, and heat transfer across the porous media becomes independent of the packing of the spheres.

Furthermore, the effect of the size of the spheres on the heat transfer has been studied by using random packings of glass spheres with diameters d = 15.3 mm and d = 10.5 mm and almost equal porosities of $\phi \sim 0.46$. Fig. 4 shows that the sphere size has a substantial effect on the heat transfer at lower Ra-numbers, with a factor ~1.5 higher heat transfer for the larger spheres at $Ra \sim 1.5\times10^7$. However, at high Ra-numbers, both curves converge, differing by less than 3% for $Ra > 6\times10^8$, and both lining up with the RB curve. This implies that the heat transfer is independent of the size of spheres if the Ra-number is sufficiently high.

The results of heat transfer measurements in the packed beds of spheres with different packing structure and sphere size showed that two heat transfer regimes can be distinguished. One is the reduced heat transfer regime at lower Ra-numbers, where the Nu-number values are lower than that of pure RB convection. In this regime, the Nu-number depends on the porous media packing and the grain size. The other regime is the *asymptotic regime*, at higher Ra-numbers, where the data from different packings and sphere sizes collapse and line up with the pure RB power-law curve with slightly higher Nu-number values. Therefore, in this regime, the heat transfer through porous media is independent of the permeability or the Darcy number. Fig. 4 also shows that the onset of the asymptotic regime is influenced by the size of the spheres in the packing bed. The onset occurs at a higher Ra-number for the smaller spheres (lower Darcy numbers).

3.1.2. Effect of Thermal Conductivity of the Spheres

Experiments were carried out with spheres made of four different materials (brass, steel, glass, polypropylene) to gain insight into the effects of the thermal properties of the spheres on the overall heat transfer. Table 1 lists the ratios of solid and fluid thermal conductivities for all combinations of solid and fluid considered in this study. Fig. 5 shows the Nu-Ra data-points obtained with 15.3 mm diameter spheres in BCT packing for the four different materials. The results show that for the entire range of Ra-numbers, Nu increases with increasing conductivity ratio. The increased heat transfer can be attributed to the increased conduction through the porous medium, which can be characterized by effective thermal conductivity of porous media.

The effective thermal conductivity is an important characteristic of a fluid-saturated porous medium. The most widely used correlations for the effective thermal conductivity of packed beds of particles are the correlations by Kunii and Smith [23] and Zehner and Schlunder [24]. These correlations were derived based on one-dimensional heat conduction models in a unit cell. Later, a modification of Zehner-Schlunder model was proposed by Hsu et al. [25]. However, these correlations were developed for the bulk region of the packed bed and are not valid in the vicinity of walls, as discussed by van Antwerpen et al. [26]. In addition, the effective thermal conductivity not only depends on the porosity and thermal conductivities of solid and fluid phases but also on the structural arrangement of the packed bed and the contact points between the solid particles [24].

Table 1. Solid to fluid conductivity ratio and the ratio of effective thermal conductivity to fluid conductivity.

Spheres and fluid materials	$\frac{k_s}{k_f}$	$\frac{k_{eff}}{k_f}$
Brass-Methanol	618	17.3
Brass-Water	196	13.6
Steel-Methanol	222	14.0
Steel-Water	70.4	9.45
Glass-Methanol	4.19	2.30
Glass-Water	1.33	1.22
Polypropylene-Methanol	1.00	1.00
Polypropylene-Water	0.32	0.79

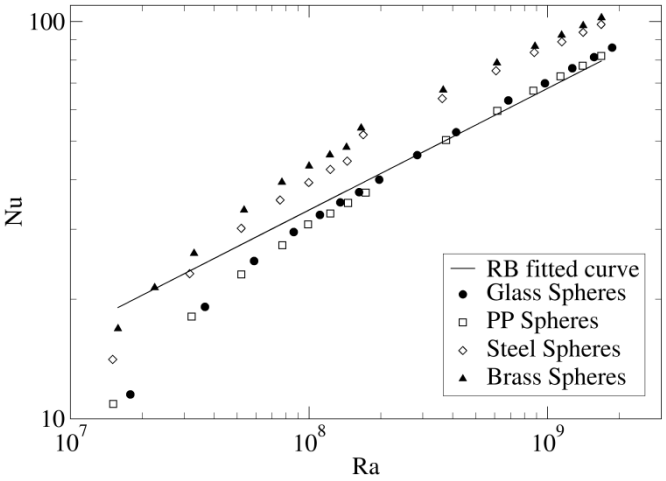

Fig. 5. Heat transfer data for BCT packing of d = 15.3 mm spheres with different thermal conductivities, compared to that for pure Rayleigh-Bénard convection.

In the absence of useable correlations for the effective conductivity, in the present work, the conduction heat transfer for exactly the same geometries as used in the experiments for each combination of fluid and sphere material was computed by solving the 3-dimensional conjugate heat conduction using the commercial CFD code ANSYS Fluent. The resulting effective conductivities are listed in Table 1.

Using the computationally determined effective thermal conductivity values k_{eff} of the various fluid-solid combinations from Table 1, we may compute the overall heat transfer due to combined conduction in the solid and fluid in the absence of convection (as e.g. in zero gravity), indicated here by $Nu_{cond} = k_{eff}/k_f$. The overall measured heat transfer, indicated by Nu, can now be split into contributions from conduction and convection, where the latter is obtained by subtracting the conduction term from the measured overall heat transfer, which gives

$$Nu_{conv} = Nu - Nu_{cond} = Nu - k_{eff}/k_f \quad (3)$$

The resulting convective Nusselt numbers N_{conv} are plotted in Fig. 6. It shows that at high Ra-numbers, the convective heat transfer data of various materials with different thermal conductivities group well together and line up with the convective pure RB curve which is given by Nu-1. Hence, the converging asymptotic regime is observed also for different conductivities, when the conduction contribution, k_{eff}/k_f, is subtracted. At lower Ra-numbers, the convective heat transfer highly depends on the conductivity of spheres and the lowest values of convective heat transfer are found for the cases with the highest conductivity of the solid spheres (brass and steel). That is mainly due to the fact that heat is primarily transported by conduction through the conductive spheres at lower Ra-numbers, enforcing a stratified temperature distribution in which convective motion of the fluid is suppressed. However, as the Ra-number increases, the convective heat transfer values for highly conductive spheres gradually approach (and in the asymptotic regime reach) those for low conductive spheres.

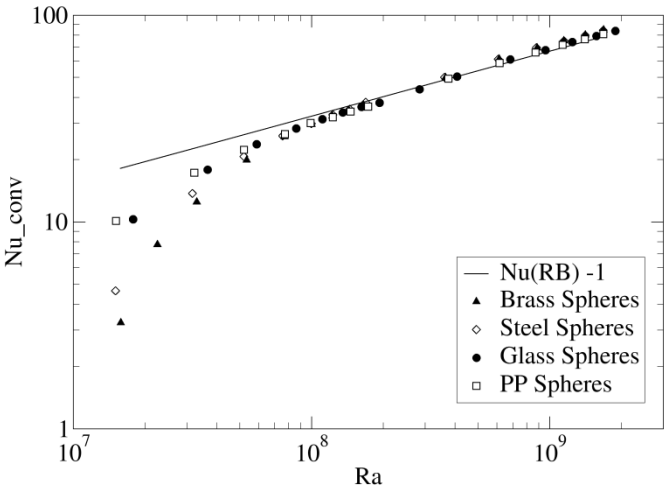

Fig. 6. Convective heat transfer for BCT packing of d = 15.3 spheres with different thermal conductivities, compared to that for pure Rayleigh-Bénard convection.

The convective heat transfer contribution for all experiments with various sphere size, packing types and conductivities are gathered in Fig. 7. This figure clearly shows the converging power-law asymptotic regime for Ra > 6×10^8 (for 15.3 mm spheres) and the reduced heat transfer regime at lower Ra-numbers. The existence of the two heat transfer regimes can be explained by comparing the thermal length scale and the porous length scale. At low Ra-numbers, in the reduced heat transfer regime, the thickness δ of the thermal boundary layers is not sufficiently small compared to the size of the spheres d. Consequently, the flow cannot penetrate into the pores easily and experiences a resistance due to the presence of the spheres. This leads to a significant reduction of the heat transfer. For highly conductive spheres, the convective heat transfer is even more suppressed due to the dominance of conduction at low Ra-numbers enforcing a stratified temperature distribution. However, at high Ra-numbers, in the asymptotic regime, the thermal boundary layers are sufficiently thin, such that the flow can penetrate into the pores and carry the heat efficiently through the porous medium regardless of packing structure, size of spheres, and their conductivity. Therefore, the convective part of heat transfer data lines up with the RB curve, and with the addition of conduction contribution, the overall heat transfer becomes even higher depending on the sphere conductivity. For the smaller spheres, the thermal boundary layer thickness δ has to become even smaller in order for the flow to penetrate into the pores. Hence the onset of the asymptotic regime occurs at higher Ra-numbers. The thermal boundary layer thickness δ is estimated by using the relation $\delta = H/(2Nu)$ and compared to the sphere sizes. The comparison of scales for all the data sets suggests that the asymptotic regime is reached when δ/d becomes less than approximately 0.045. To confirm the above-mentioned explanation, the velocity and temperature fields of the two heat transfer regimes are compared in the next section.

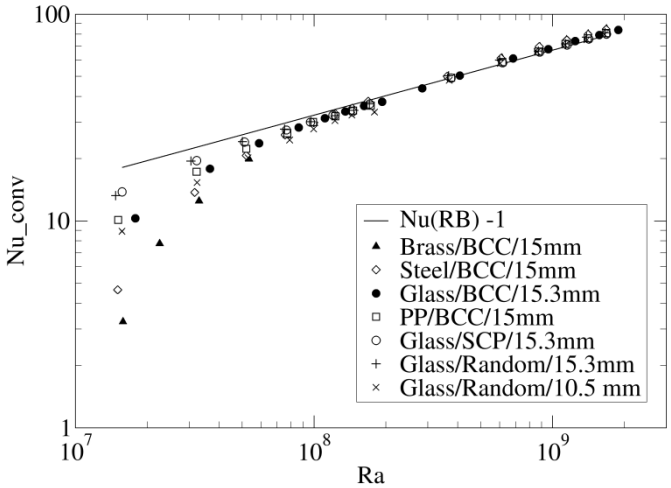

Fig. 7. Convective heat transfer for different sphere conductivities, packing types, and sphere sizes, compared to that for pure Rayleigh-Bénard convection.

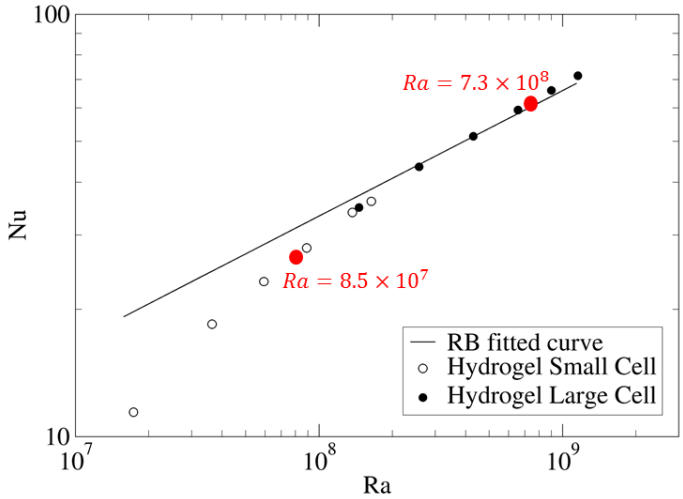

Fig. 8. Convective heat transfer for Hydrogel spheres in water. PIV/LCT measurement points are shown in red.

3.2. Results of the PIV and LCT measurements

To better understand the physics of natural convection flow in coarse-grained porous media and enhance knowledge of the mechanisms influencing the heat transfer in the two regimes, velocity and temperature fields were measured at two different Ra-numbers, i.e. Ra = 8.5×10^7 which is in the reduced heat transfer regime and Ra = 7.3×10^8 which is in the asymptotic regime. Fig. 8 shows the Nu-Ra data-points for BCT packing of 15.3 mm hydrogel spheres in water, and the two data-points where the velocity and temperature measurements were carried out.

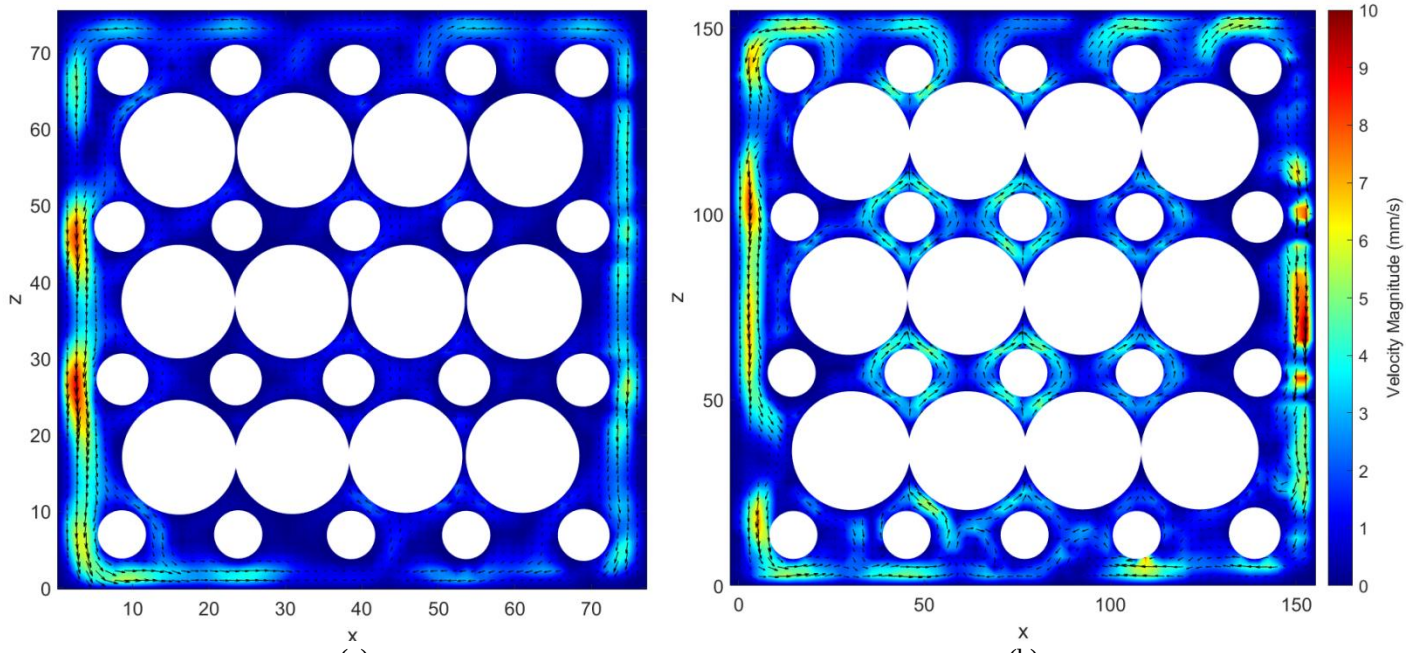

(a) (b)

Fig. 9. Mean velocity fields in a vertical plane at (a) Ra = 8.5×10^7 and (b) Ra = 7.3×10^8.

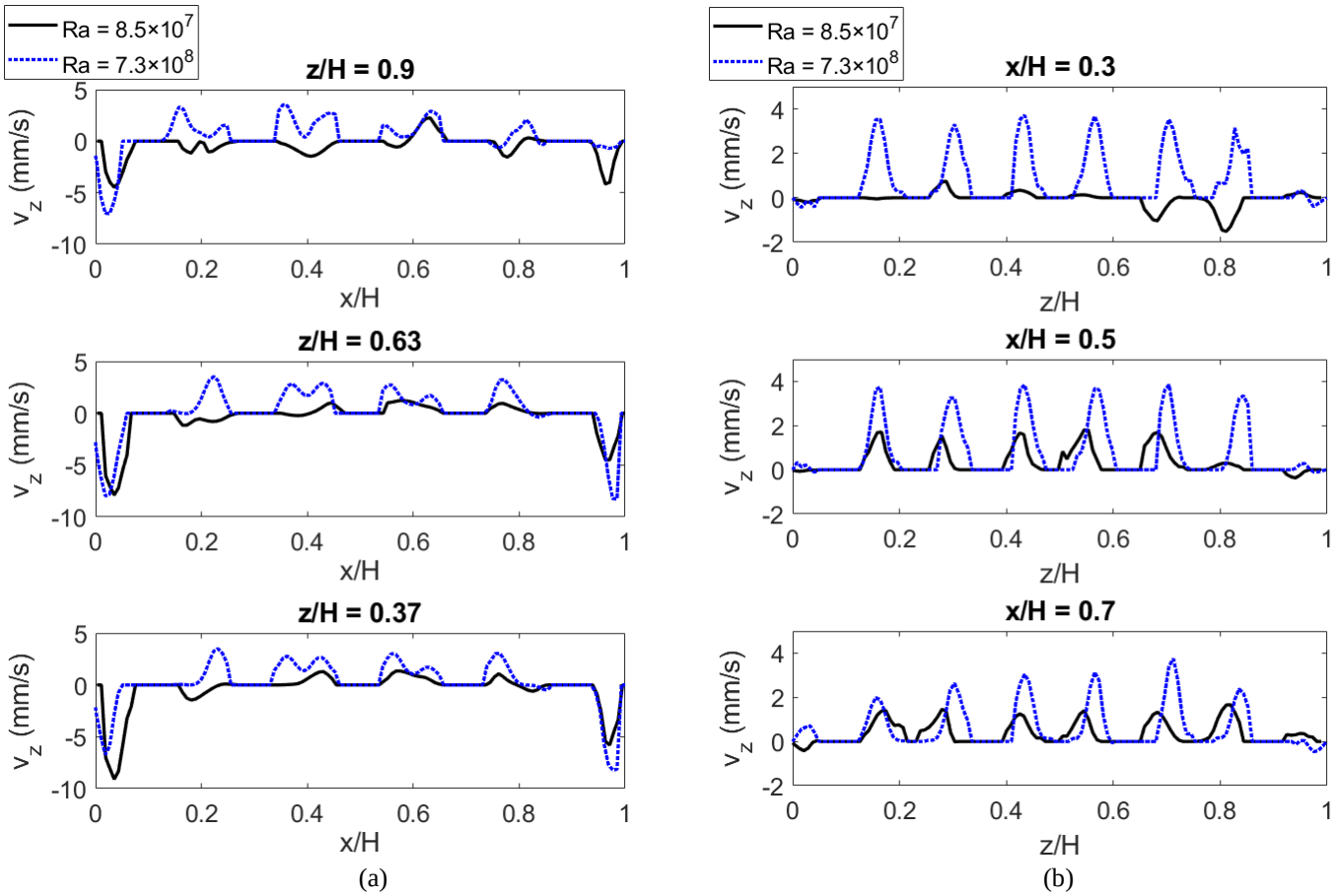

(a) (b)

Fig. 10. Profiles of the mean vertical velocity component for Ra = 8.5×10^7 (black line) and Ra = 7.3×10^8 (blue dotted line) along (a) three different horizontal lines (z/H = 0.37, z/H = 0.63, and z/H = 0.90) and (b) three different vertical lines (x/H = 0.3, x/H = 0.5, and x/H = 0.7)

Water and hydrogel form a fully transparent refractive index matched liquid-solid pair that enabled the use of the optical measurement techniques, PIV and LCT, to study natural convection velocity and temperature fields in porous media for the first time. Fig. 9 shows the mean velocity fields for the reduced heat transfer regime at Ra = 8.5×10^7 (left) and the asymptotic regime at Ra = 7.3×10^8 (right). The mean velocity fields were determined from 10000 double snapshots that were acquired at a frequency of 1 Hz. The velocity vectors are shown in black and are overlaid on a color map which describes the local velocity magnitude. The velocity fields clearly show that at Ra = 8.5×10^7, in the reduced heat transfer regime, the flow velocities in the central region inside the pores are very small, whereas flow with high velocity is observed only in a thin layer near the periphery of the cell. However, at Ra = 7.3×10^8, in the asymptotic regime, high velocities occur inside the pores as well as near the walls. To make a better and more quantitative comparison of the local velocity distribution at the two different Ra-numbers, vertical velocity component (v_z) profiles along three different horizontal lines $z/H = 0.37$, $z/H = 0.63$, and $z/H = 0.90$ and also along three different vertical lines $x/H = 0.3$, $x/H = 0.5$, and $x/H = 0.7$ are shown in Fig. 10. The increased penetrating velocities in the pores at the higher Ra-number is clearly observed at various vertical and horizontal positions, whereas near-wall velocities remained almost unchanged.

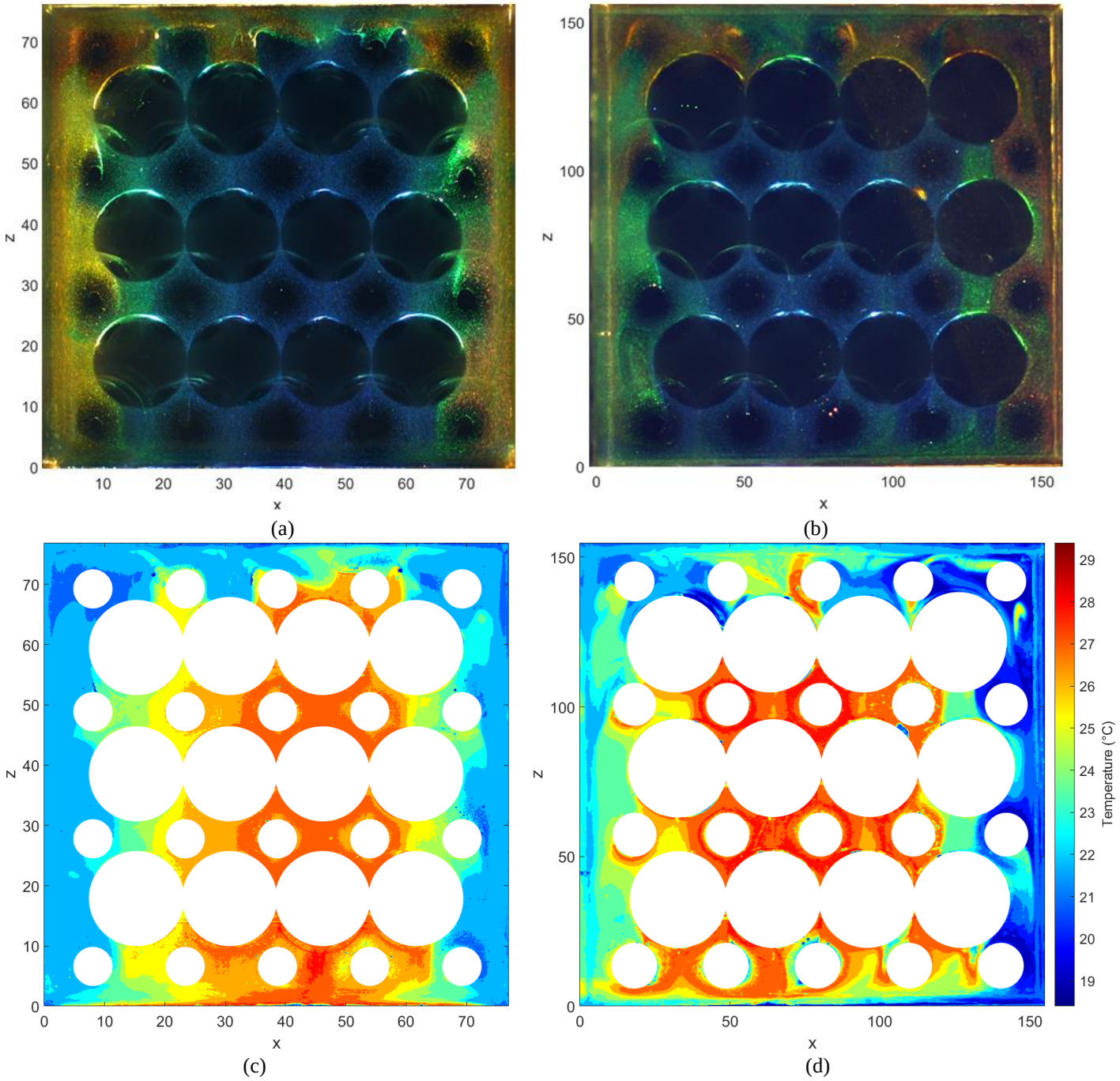

Fig. 11. Qualitative instantaneous temperature distribution at (a) Ra = 8.5×10^7 and (b) Ra = 7.3×10^8. In these images, the red color corresponds to the lowest temperature and the blue color represents the highest temperature. Quantitative mean temperature distribution at (c) Ra = 8.5×10^7 and (d) Ra = 7.3×10^8. In these measurements, the temperatures of the cooling and heating plates were set to 18.4 °C and 29.4 °C, respectively.

The overall mean velocity fields and the local mean velocity profiles obtained by PIV experiments clearly supports the explanation that the ratio between the thermal length scales and pore length scales determines the flow structure and heat transfer in porous media. At low Ra-numbers, δ/d is not sufficiently small, therefore the flow cannot easily penetrate into the pores and it prefers to move along the walls where more space is available due to higher local porosity. However, in the asymptotic regime, δ/d becomes sufficiently small such that the flow can penetrate into the pores with high velocities and carry the heat to the opposite plate without experiencing resistance from the presence of the spheres, and the convection heat transfer can reach values as high as those in RB convection.

Fig. 11 shows the qualitative and quantitative steady state temperature distributions obtained from LCT measurements at Ra = 8.5×10^7 (left) and Ra = 7.3×10^8 (right). At both Ra-numbers, the temperatures of the cooling and heating plates were set to 18.4 °C and 29.4 °C, respectively. In the qualitative images, the red color corresponds to the lowest temperature and the blue color represents the highest temperature. The obtained temperature fields show that at both studied Ra-numbers, warmer fluid moves upward in the central region (hot core) and colder fluid moves downward near the side walls. These vertical columnar structures spanning the height of the cell were also observed by Hewitt et al. [27] in their 2D direct numerical simulation using Darcy's law, and were called "mega plumes".

Despite the similarities in flow structure, some differences can be also observed. The most important one is that at high Ra-number, relatively cold fluid can be observed just adjacent to the heating plate, and also hot fluid very close to the cooling plate. This means that hot and cold fluid can penetrate very deeply up to the opposite solid boundaries and consequently enhance the heat transfer. That is mainly due to the much higher penetrating velocities through the porous medium which enhance the strength of thermal advection compared to thermal diffusion. However, at low Ra-number the heat diffuses to a greater extent from the hot central region to the cold regions along the side walls, leading to a narrower temperature range in the cell.

Overall, the flow and temperature visualization results confirm that the ratio between the thermal boundary layer thickness and the sphere size determines the flow structure and subsequently governs the corresponding heat transfer to be either in the reduced heat transfer regime or in the asymptotic regime. Therefore, the comparison between thermal length scales and porous length scales plays a central role in natural convection flow in porous media.

4. Conclusions

An experimental study of bottom-heated natural convection in coarse-grained porous media, where the porous length scale is not small compared to the flow and thermal length scales, was carried out. Nusselt numbers were measured for various sphere conductivities, spheres sizes, and sphere packings at Rayleigh numbers between 10^7 and 10^9. Particle image velocimetry and liquid crystal thermography were used to determine planar velocity and temperature fields in the natural convection cell filled with porous media by using water and hydrogel as refractive index matched pairs.

Nusselt number measurements showed two heat transfer regimes: (i) reduced heat transfer regime at lower Rayleigh numbers, and (ii) asymptotic regime at higher Rayleigh numbers. The Nusselt numbers in the asymptotic regime are independent of packing type and sphere size but clearly depend on the conductivity ratio of the fluid and porous medium. However, the convective contribution of heat transfer converges and lines up with the curve for pure Rayleigh-Bénard convection, for all sphere conductivities, sizes, and packings.

Visualization of the velocity and temperature fields of the two heat transfer regimes showed that in the reduced heat transfer regime, the flow hardly penetrates into the pores, and it is mostly confined to a (thin) region along the periphery of the cell. However, in the asymptotic regime, since the thermal boundary layers become sufficiently thin, the flow penetrates considerably into the porous layer leading to much higher velocity magnitudes in the core region, a deeper penetration of hot and cold fluid up to the opposite solid boundaries, and consequently higher heat transfer across the porous medium. The obtained results confirm that the comparison between thermal length scales and porous length scales determine the flow structure and the corresponding heat transfer in natural convection in porous media.

Conflict of Interest

There is no conflict of interest associated with this publication.

Acknowledgements

This research was carried out under project number S41.5.14526 in the framework of the Partnership Program of the Material innovation institute M2i (www.m2i.nl) and the Technology Foundation TTW (www.stw.nl), which is part of the Netherlands Organization for Scientific Research (www.nwo.nl). We also acknowledge the support of Tata Steel Europe. We thank Bart Hoek for his technical support in preparation of the experiments.

Appendix A. Uncertainty Analysis

The uncertainty values were obtained by propagation of error analysis. For the Ra-number defined in Eq. (2), the maximum uncertainty was measured at the lowest ΔT as

$$\frac{\mathrm{dRa}}{\mathrm{Ra}} = \sqrt{\left(\frac{\mathrm{d}\beta}{\beta}\right)^2 + \left(\frac{\mathrm{d}\alpha}{\alpha}\right)^2 + \left(\frac{\mathrm{d}\nu}{\nu}\right)^2 + \left(\frac{\mathrm{d}g}{g}\right)^2 + \left(\frac{\mathrm{d}\Delta T}{\Delta T}\right)^2 + \left(3\frac{\mathrm{d}H}{H}\right)^2} = 2.8\% \tag{4}$$

For the Nu-number defined in Eq. (1) as $\mathrm{Nu} = IVH/(A_f k_f \Delta T) - A_w k_w/(A_f k_f)$, where I and V are the electrical current and voltage fed to the heating foils, $A_f = H^2$ and $A_w = 4w(H+w)$, the maximum uncertainty was measured as

$$\frac{\mathrm{d}\left(\frac{I\,V\,H}{A_f\,k_f\,\Delta T}\right)}{\frac{I\,V\,H}{A_f\,k_f\,\Delta T}} = \sqrt{\left(\frac{\mathrm{d}I}{I}\right)^2 + \left(\frac{\mathrm{d}V}{V}\right)^2 + \left(\frac{\mathrm{d}H}{H}\right)^2 + \left(2\frac{\mathrm{d}H}{H}\right)^2 + \left(\frac{\mathrm{d}\Delta T}{\Delta T}\right)^2 + \left(\frac{\mathrm{d}k_f}{k_f}\right)^2} \tag{5}$$

$$\frac{\mathrm{d}\left(\frac{(H+w)\,w\,k_\mathrm{w}}{A_\mathrm{f}\,k_\mathrm{f}}\right)}{\frac{(H+w)\,w\,k_\mathrm{w}}{A_\mathrm{f}\,k_\mathrm{f}}} = \sqrt{\left(\frac{\mathrm{d}(H+w)}{H+w}\right)^2 + \left(\frac{\mathrm{d}w}{w}\right)^2 + \left(2\frac{\mathrm{d}H}{H}\right)^2 + \left(\frac{\mathrm{d}k_\mathrm{f}}{k_\mathrm{f}}\right)^2 + \left(\frac{\mathrm{d}k_\mathrm{w}}{k_\mathrm{w}}\right)^2} \tag{6}$$

$$\frac{\mathrm{dNu}}{\mathrm{Nu}} = \frac{\sqrt{\left(\mathrm{d}\left(\frac{I\,V\,H}{A_\mathrm{f}\,k_\mathrm{f}\,\Delta T}\right)\right)^2 + \left(4\,\mathrm{d}\left(\frac{(H+w)\,w\,k_\mathrm{w}}{A_\mathrm{f}\,k_\mathrm{f}}\right)\right)^2}}{\mathrm{Nu}} = 2.9\% \tag{7}$$

The calculated maximum uncertainty (at the lowest ΔT) is 2.9% for Nu-number and 2.8% for Ra-number.

In these calculations, the uncertainty in each of the fluid properties was assumed to be 1% i.e. $\mathrm{d}\beta/\beta = \mathrm{d}\alpha/\alpha = \mathrm{d}\nu/\nu = \mathrm{d}k_\mathrm{f}/k_\mathrm{f} = \mathrm{d}k_\mathrm{w}/k_\mathrm{w} = 0.01$. The uncertainty of the voltage and the current supplied to the heating foil are $\mathrm{d}V = 0.005$ Volt and $\mathrm{d}I/I = 1\%$. The uncertainty of measuring any length is $\mathrm{d}H = \mathrm{d}w = \mathrm{d}(L+w) = 0.1$ mm. The uncertainties in the measured $\Delta T = T_\mathrm{h} - T_\mathrm{c}$ is $\mathrm{d}\Delta T = 0.05$ °C which was calculated as follows. The inaccuracy of the Pt100 temperature sensors is ±0.03 °C. The maximum temperature non-uniformity was ~ 0.04 °C for the heating plate and ~ 0.01 °C for the cooling plate. For all our measurements the average of two temperature sensors in each plate was used as the plate temperature. Therefore, the uncertainty due to temperature non-uniformity is $0.04/\sqrt{2}$ °C for T_hot and $0.01/\sqrt{2}$ °C for T_cold. The overall uncertainty in measuring $\Delta T = T_\mathrm{hot} - T_\mathrm{cold}$ is $(0.03^2 + (0.04/\sqrt{2})^2 + 0.03^2 + (0.01/\sqrt{2}\ ^\circ\mathrm{C})^2)^{1/2} \cong 0.05$ °C.

References

[1] E.R. Lapwood, Convection of a fluid in a porous medium, Math. Proc. Cambridge Philos. Soc. 44 (1948) 508. doi:10.1017/S030500410002452X.

[2] D.R. Hewitt, J.A. Neufeld, J.R. Lister, High Rayleigh number convection in a three-dimensional porous medium, J. Fluid Mech. 748 (2014) 879–895. doi:10.1017/jfm.2014.216.

[3] J. Otero, L.A. Dontcheva, H. Johnston, R.A. Worthing, A. Kurganov, G. Petrova, C.R. Doering, High-Rayleigh-number convection in a fluid-saturated porous layer, J. Fluid Mech. 500 (2004) 263–281. doi:10.1017/S0022112003007298.

[4] R.A. Wooding, Steady state free thermal convection of liquid in a saturated permeable medium, J. Fluid Mech. 2 (1957) 273. doi:10.1017/S0022112057000129.

[5] D.D. Joseph, D.A. Nield, G. Papanicolaou, Nonlinear equation governing flow in a saturated porous medium, Water Resour. Res. 18 (1982) 1049–1052. doi:10.1029/WR018i004p01049.

[6] J.W. Elder, Steady free convection in a porous medium heated from below, J. Fluid Mech. 27 (1967) 29. doi:10.1017/S0022112067000023.

[7] C.R.B. Lister, An explanation for the multivalued heat transport found experimentally for convection in a porous medium, J. Fluid Mech. 214 (1990) 287. doi:10.1017/S0022112090000143.

[8] N. Kladias, V. Prasad, Experimental verification of Darcy-Brinkman-Forchheimer flow model for natural convection in porous media, J. Thermophys. Heat Transf. 5 (1991) 560–576. doi:10.2514/3.301.

[9] D.J. Keene, R.J. Goldstein, Thermal Convection in Porous Media at High Rayleigh Numbers, J. Heat Transfer. 137 (2015) 034503. doi:10.1115/1.4029087.

[10] H. Lein, R.S. Tankin, Natural convection in porous media—I. Nonfreezing, Int. J. Heat Mass Transf. 35 (1992) 175–186. doi:10.1016/0017-9310(92)90018-N.

[11] L.E. Howle, R.P. Behringer, J.G. Georgiadis, Convection and flow in porous media. Part 2. Visualization by shadowgraph, J. Fluid Mech. 332 (1997) 247–262. doi:10.1017/S0022112096004004.

[12] V. Prasad, F.A. Kulacki, M. Keyhani, Natural convection in porous media, J. Fluid Mech. 150 (1985) 89. doi:10.1017/S0022112085000040.

[13] M.D. Shattuck, R.P. Behringer, G.A. Johnson, J.G. Georgiadis, Convection and flow in porous media. Part 1. Visualization by magnetic resonance imaging, J. Fluid Mech. 332 (1997) 215–245. doi:10.1017/S0022112096003990.

[14] K. Bai, J. Katz, On the refractive index of sodium iodide solutions for index matching in PIV, Exp. Fluids. 55 (2014) 1704. doi:10.1007/s00348-014-1704-x.

[15] R. Häfeli, M. Altheimer, D. Butscher, P. Rudolf von Rohr, PIV study of flow through porous structure using refractive index matching, Exp. Fluids. 55 (2014) 1717. doi:10.1007/s00348-014-1717-5.

[16] Y.A. Hassan, E.E. Dominguez-Ontiveros, Flow visualization in a pebble bed reactor experiment using PIV and refractive index matching techniques, Nucl. Eng. Des. 238 (2008) 3080–3085. doi:10.1016/J.NUCENGDES.2008.01.027.

[17] D. Butscher, C. Hutter, S. Kuhn, P. Rudolf von Rohr, Particle image velocimetry in a foam-like porous structure using refractive index matching: a method to characterize the hydrodynamic performance of porous structures, Exp. Fluids. 53 (2012) 1123–1132. doi:10.1007/s00348-012-1346-9.

[18] M.L. Byron, E.A. Variano, Refractive-index-matched hydrogel materials for measuring flow-structure interactions, Exp. Fluids. 54 (2013) 1456. doi:10.1007/s00348-013-1456-z.

[19] J.S. Weitzman, L.C. Samuel, A.E. Craig, R.B. Zeller, S.G. Monismith, J.R. Koseff, On the use of refractive-index-matched hydrogel for fluid velocity measurement within and around geometrically complex solid obstructions, Exp. Fluids. 55 (2014) 1862. doi:10.1007/s00348-014-1862-x.

[20] S. Klein, M. Gibert, A. Bérut, E. Bodenschatz, Simultaneous 3D measurement of the translation and rotation of finite-size particles and the flow field in a fully developed turbulent water flow, Meas. Sci. Technol. 24 (2013) 024006. doi:10.1088/0957-0233/24/2/024006.

[21] A.R. Smith, Color gamut transform pairs, ACM SIGGRAPH Comput. Graph. 12 (1978) 12–19. doi:10.1145/965139.807361.

[22] S. Grossmann, D. Lohse, Scaling in thermal convection: a unifying theory, J. Fluid Mech. 407 (2000) S0022112099007545. doi:10.1017/S0022112099007545.

[23] D. Kunii, J.M. Smith, Heat transfer characteristics of porous rocks, AIChE J. 6 (1960) 71–78. doi:10.1002/aic.690060115.

[24] P. Zehner, E.U. Schlünder, Wärmeleitfähigkeit von Schüttungen bei mäßigen Temperaturen, Chemie Ing. Tech. 42 (1970) 933–941. doi:10.1002/cite.330421408.

[25] C.T. Hsu, P. Cheng, K.W. Wong, Modified Zehner-Schlunder models for stagnant thermal conductivity of porous media, Int. J. Heat Mass Transf. 37 (1994) 2751–2759. doi:10.1016/0017-9310(94)90392-1.

[26] W. van Antwerpen, C.G. du Toit, P.G. Rousseau, A review of correlations to model the packing structure and effective thermal conductivity in packed beds of mono-sized spherical particles, Nucl. Eng. Des. 240 (2010) 1803–1818. doi:10.1016/J.NUCENGDES.2010.03.009.

[27] D.R. Hewitt, J.A. Neufeld, J.R. Lister, Ultimate Regime of High Rayleigh Number Convection in a Porous Medium, Phys. Rev. Lett. 108 (2012) 224503. doi:10.1103/PhysRevLett.108.224503.